Atomic scattering from an adsorbed monolayer solid with a helium beam that penetrates to the substrate

Hansen, Flemming Yssing; Bruch, L.W.; Dammann, Bernd

Published in:
Journal of Chemical Physics

Link to article, DOI:
10.1063/1.4794742

Publication date:
2013

Document Version
Publisher's PDF, also known as Version of record

Atomic scattering from an adsorbed monolayer solid with a helium beam that penetrates to the substrate

F. Y. Hansen, L. W. Bruch, and B. Dammann

Citation: J. Chem. Phys. **138**, 104705 (2013); doi: 10.1063/1.4794742
View online: http://dx.doi.org/10.1063/1.4794742
View Table of Contents: http://jcp.aip.org/resource/1/JCPSA6/v138/i10
Published by the American Institute of Physics.

Atomic scattering from an adsorbed monolayer solid with a helium beam that penetrates to the substrate

F. Y. Hansen,[1,a)] L. W. Bruch,[2] and B. Dammann[3]
[1]*Department of Chemistry, Technical University of Denmark, IK-207-DTU, DK-2800 Lyngby, Denmark*
[2]*Department of Physics, University of Wisconsin–Madison, 1150 University Avenue, Madison, Wisconsin 53706, USA*
[3]*Department of Informatics and Mathematical Modeling, Technical University of Denmark, 321-DTU, DK 2800 Lyngby, Denmark*

(Received 18 December 2012; accepted 22 February 2013; published online 14 March 2013)

Diffraction and one-phonon inelastic scattering of a thermal energy helium atomic beam are evaluated in the situation that the target monolayer lattice is so dilated that the atomic beam penetrates to the interlayer region between the monolayer and the substrate. The scattering is simulated by propagating a wavepacket and including the effect of a feedback of the inelastic wave onto the diffracted wave, which represents a coherent re-absorption of the created phonons. Parameters are chosen to be representative of an observed $p(1 \times 1)$ commensurate monolayer solid of H_2/NaCl(001) and a conjectured $p(1 \times 1)$ commensurate monolayer solid of H_2/KCl(001). For the latter, there are cases where part of the incident beam is trapped in the interlayer region for times exceeding 50 ps, depending on the spacing between the monolayer and the substrate and on the angle of incidence. The feedback effect is large for cases of strong transient trapping. © *2013 American Institute of Physics*. [http://dx.doi.org/10.1063/1.4794742]

I. INTRODUCTION

Inelastic helium atom scattering experiments have determined the energies of phonons in physically adsorbed monolayer solids.[1,2] The theory is relatively complex because the processes that make a thermal energy He beam an exquisitely surface sensitive probe require treating the scattering as a strong coupling event.[3–6] For example, the simply commensurate monolayer solid $p(1 \times 1)$ H_2/NaCl(001) is such a corrugated target that some experimental diffraction peaks are more intense than the specular peak[7] and the theory[6] shows this too. Further, that monolayer solid is so dilated that there is only a low potential energy barrier for the He to penetrate to the interlayer region that is between the plane of the monolayer molecule centers and the plane of the centers of surface ions of the substrate and there may be paths with no barrier for a more dilated conjectured commensurate monolayer solid $p(1 \times 1)$ H_2/KCl(001) that has not yet been observed.

We anticipated that there would be strong transient trapping in the interlayer region for He scattering from $p(1 \times 1)$ H_2/KCl(001) and found in trial calculations that the wavepacket scattering methodology extended stably to such conditions. However, the strong coupling effects are enhanced for the wave function in the interlayer region. Therefore, we have generalized the one-phonon scattering theory to include a feedback of the inelastic wave function onto the elastic (diffracted) wave function, in which the created phonon is coherently annihilated. This provides a self-consistent (SC) description of the scattering process in the zero and one phonon space and maintains conservation of total probability.

We have re-visited the $p(1 \times 1)$ H_2/NaCl(001) system, because including the barrier penetration effect satisfactorily removes a norm loss artifact in the calculations of Ref. 6, denoted as Paper III here. There are only minor changes from the previously calculated inelastic scattering distributions. For this system there are good models[8–10] for the He–H_2 and He–NaCl interactions and experimental data[7] for the phonon spectrum. In contrast, the components of the interaction model for the H_2/KCl(001) are less well-determined and the calculations there are more exploratory in character. As yet, there are no inelastic helium atom scattering experiments that show effects of large penetration to the interlayer region between monolayer and substrate. This is in marked contrast to low energy electron diffraction experiments, where interference between reflections at the monolayer and at the substrate is analyzed to determine the adsorption-site geometry.[11]

Our previous work (Papers I–III)[4–6] is in the context of the time-dependent evolution of a scattering wave packet and starts from the one-phonon scattering approximation of Choi and Poe.[12] The time-dependent theory exhibits the dynamic interplay of the elastic and inelastic processes. There also is a large body of work[3] on helium atom scattering from physically adsorbed monolayers that uses a time-independent coupled-channel formulation. From its beginning,[13] approximate solutions were constructed which conserved total probability (unitarity) and that was implemented with averaged approximations for the Debye-Waller factor. According to a recent example of such work,[14] our self-consistent one-phonon calculations may over-estimate the effect of one-phonon losses; this is likely to become a large effect for multiphonon scattering[3] which we do not treat here. Another related effect is the phonon-assisted resonances[15,16] in which one-phonon processes enhance selective adsorption

a)Author to whom correspondence should be addressed. Electronic mail: flemming@kemi.dtu.dk.

resonances in the diffracted wave. Although the cases in our model calculation are not at the resonant condition, there are long transient trapping times that suggest a proximity to such effects. The role of thermal excitation of the monolayer and dynamics of the substrate is not yet incorporated in our work. We believe that this may be done more easily in the time-dependent theory than in the time-independent formulation but that the two approaches have an important complementarity. As calculations are extended to higher energies where multiphonon processes contribute more, semi-classical approximations[17] will play a larger role.

The organization of this paper is as follows: Sec. II summarizes the theoretical components of this work, the potential models, and the scattering theory. Section III presents the results of the calculations. Section IV contains the conclusions. The Appendix summarizes a ray tracing (geometrical optics) approximation for the penetration of He to the interlayer region.

II. THEORY

A. Self-consistent one-phonon approximation

The Hamiltonian for scattering of an atom by the monolayer solid is

$$H = K_{\rm kin} + H_{\rm ph} + V_c. \tag{1}$$

$K_{\rm kin}$ is the kinetic energy operator of the incident (He) atom of mass m_a. $H_{\rm ph}$ is the Hamiltonian of the monolayer solid treated in the harmonic approximation and is expressed in phonon operators by

$$H_{\rm ph} = \sum_{\mathbf{Q},\lambda} \hbar\omega(\mathbf{Q},\lambda) a^+(\mathbf{Q},\lambda) a(\mathbf{Q},\lambda), \tag{2}$$

with a sum over wavevectors $\mathbf{Q}$ in the first Brillouin zone and polarization branches λ. The ground state of $H_{\rm ph}$ is denoted Φ_0, with energy zero, i.e., zero-point energies are omitted. V_c denotes the sum of the atom-monolayer and atom-substrate potential energies. It consists of a static part V_s with all monolayer and substrate atoms at their equilibrium positions and a dynamic part V_d arising from the vibrational displacements of the monolayer atoms. Dynamic coupling of the monolayer and substrate is neglected and V_d is approximated by V_1, its expansion to first order in monolayer atom displacements and phonon operators:

$$V_d \simeq V_1 = \sum_{\mathbf{Q},\lambda} \tilde{V}_{\mathbf{Q},\lambda} a^+(\mathbf{Q},\lambda) + \tilde{V}^*_{\mathbf{Q},\lambda} a(\mathbf{Q},\lambda). \tag{3}$$

The time-dependent Schrödinger equation then is

$$\imath\hbar \frac{\partial \Psi}{\partial t} = (H_0 + H_{\rm ph} + V_1)\Psi, \tag{4}$$

with $H_0 = K_{\rm kin} + V_s$. Assuming a solution of the form $\Psi = \Psi_0\Phi_0 + \sum_{\mathbf{Q},\lambda} \Psi_1(\mathbf{Q},\lambda) a^+(\mathbf{Q},\lambda)\Phi_0$ and projecting Eq. (4) onto the zero-phonon (Φ_0) and one-phonon ($a^+(\mathbf{Q},\lambda)\Phi_0$) spaces gives coupled equations for the scattered-atom wave functions Ψ_0 and Ψ_1

$$\imath\hbar \frac{\partial \Psi_0}{\partial t} = H_0\Psi_0 + \sum_{\mathbf{Q},\lambda} \tilde{V}^*_{\mathbf{Q},\lambda} \Psi_1(\mathbf{Q},\lambda) \tag{5}$$

and

$$\imath\hbar \frac{\partial \Psi_1(\mathbf{Q},\lambda)}{\partial t} = [H_0 + \hbar\omega(\mathbf{Q},\lambda)]\Psi_1(\mathbf{Q},\lambda) + \tilde{V}_{\mathbf{Q},\lambda}\Psi_0. \tag{6}$$

There is an Eq. (6) for each ($\mathbf{Q}$, λ) in the sum in Eq. (5). Multiphonon processes are neglected and the phonon states are those of the unperturbed monolayer. The total norm is conserved for this set of dynamical equations:

$$(\Psi_0+\Psi_1, \Psi_0+\Psi_1) = (\Psi_0, \Psi_0) + (\Psi_1, \Psi_1) = \int [|\Psi_0|^2 + \sum_{\mathbf{Q},\lambda} |\Psi_1(\mathbf{Q},\lambda)|^2] dx dy dz = 1. \tag{7}$$

In a scattering event with initial condition $\Psi_1 = 0$ and the monolayer initially in the state Φ_0, the last term in Eq. (6) usually acts as a source term. There are time periods where its action is more complex and the norm of Ψ_1 does not increase monotonically with time. The $\tilde{V}^*_{\mathbf{Q},\lambda}$ term in Eq. (5) represents the feedback of the inelastic scattering onto the elastic (diffraction) scattering and leads to a reduction in the norm of Ψ_0 from the initial value of one. This self-consistency represents one of the processes in the Debye-Waller factor for diffraction intensities.[3] We denote solutions of Eqs. (5) and (6) by SC and those in which the $\tilde{V}^*_{\mathbf{Q},\lambda}$ term is omitted from Eq. (5), as in Paper III, by NSC (non-self-consistent).

The lateral, $\mathbf{r} = (x, y)$, periodicities of the potential energies $V_s(\mathbf{r}, z)$ and $\tilde{V}_{\mathbf{Q},\lambda}(\mathbf{r}, z)$ are expanded in the Steele series[19] using the reciprocal lattice vectors $\mathbf{g}$ of the monolayer. The corresponding expansions of the zero-phonon and one-phonon atom wave functions Ψ_0 and Ψ_1 are, with $\mathbf{K}$ the initial parallel wavevector of the atom,

$$\Psi_0 = \sum_{\mathbf{g}} \psi_{\mathbf{g}}(z,t) \exp[\imath(\mathbf{g}+\mathbf{K})\cdot\mathbf{r}] \tag{8}$$

and

$$\Psi_1(\mathbf{Q},\lambda) = \sum_{\mathbf{g}} \exp[\imath(\mathbf{K}-\mathbf{Q}+\mathbf{g})\cdot\mathbf{r}] S_{\mathbf{Q},\lambda}(\mathbf{g},z,t). \tag{9}$$

B. Implementation: Helium atom scattering

1. Interaction models

The interaction of the He atom with an H_2 molecule is taken to be the TSM model (Tao[8] and Spelsberg-Meyer[9]) without zero-point averaging, as given in Paper III. However, in evaluating the coefficients in the Steele series, a cutoff procedure is adopted for small separations because the numerical integration of Eqs. (5) and (6) becomes unstable for very large potential energies. A smooth cutoff is used at separations r less than a value r_s:

$$V(r) = V_{\rm TSM}(r) \times \exp(-\gamma_2[r - r_s]^2), \quad r \le r_s. \tag{10}$$

With the choices $r_s = 1.5$ Å and $\gamma_2 = 0.421$ Å^{-2}, the maximum of V(r) is limited to 13.1 eV and the wavepacket propagates stably even when a significant amount penetrates to the interlayer region between the monolayer and the substrate. Since the He beam energies considered are in the range

8–26 meV, this cutoff on $V(r)$ is unlikely to give spurious effects in the scattering calculation. The He-monolayer potential is the sum of V_{TSM} or V over a square lattice of H_2 molecules with nearest-neighbor spacing $L_{nn} = 3.96$ Å [4.44 Å] for the NaCl(001) [KCl(001)] case.

The interaction of He with NaCl(001) was modeled by Vargas and Mochán.[10] In Paper III, the effective surface plane of the NaCl is taken to be $DZL = 1.2$ Å below the H_2 monolayer; the actual distance from the H_2 monolayer to the NaCl(001) is calculated[18] to be 2.6 Å. A similar construction for He–KCl(001) is not available, but the selective adsorption energy levels are known[7] to be very similar to those for He–NaCl(001). As an estimate of the He–KCl(001) potential we adopt the Vargas-Mochán model and use three values for DZL (1.2, 2.8, and 4.0 Å). The larger values lead to transient configurations with large interlayer components in both Ψ_0 and Ψ_1 and enable us to examine trapping effects quite readily.

The potential energy surfaces are approximated by Steele series with NVG = 25 [30] shells of reciprocal lattice vectors for the NaCl [KCl] case and are constrained by a Lagrange multiplier construction[6] to match the direct sum evaluations at the atop, center, and bridge sites of the unit cell for each perpendicular distance z from the hydrogen monolayer. Contour plots of the He-$p(1 \times 1)H_2$/KCl(001) potential energy in the $z = 0$ plane (the plane of H_2 centers) for $DZL = 1.2$ Å and 4.0 Å are shown for one unit cell in Fig. 1. The two plots illustrate that the "hole" (area with a negative potential energy) at the center of the cell is larger for $DZL = 1.2$ Å than for $DZL = 4.0$ Å. This arises because the attractive part of the He–KCl potential energy at $z = 0$ is larger for $DZL = 1.2$ Å where the KCl surface is closer. However, the effects of the $z < 0$ region are larger in the scattering calculations for $DZL = 4.0$ Å because the larger volume of this region outweighs the effect of the larger "hole" in the $z = 0$ plane for $DZL = 1.2$ Å.

In Paper III the closest approach of He to the $p(1 \times 1)H_2$/NaCl(001) monolayer was $z = 0.4$ Å and there was a loss of up to 1.5% in the norm of Ψ_0 because the potential energy in part of the $z = 0.4$ Å plane is less than the initial beam energy E_i. The potential energy at the unit cell center at $z = 0$ is 1.8 meV for the NaCl case and is in the range -5 to -13 meV, depending on DZL, for the KCl cases. The large potential energy at $z = -DZL$ has the effect of reducing the loss of total norm (elastic + inelastic, $I_e + I_i$, Eq. (7)) to less than 0.1%.

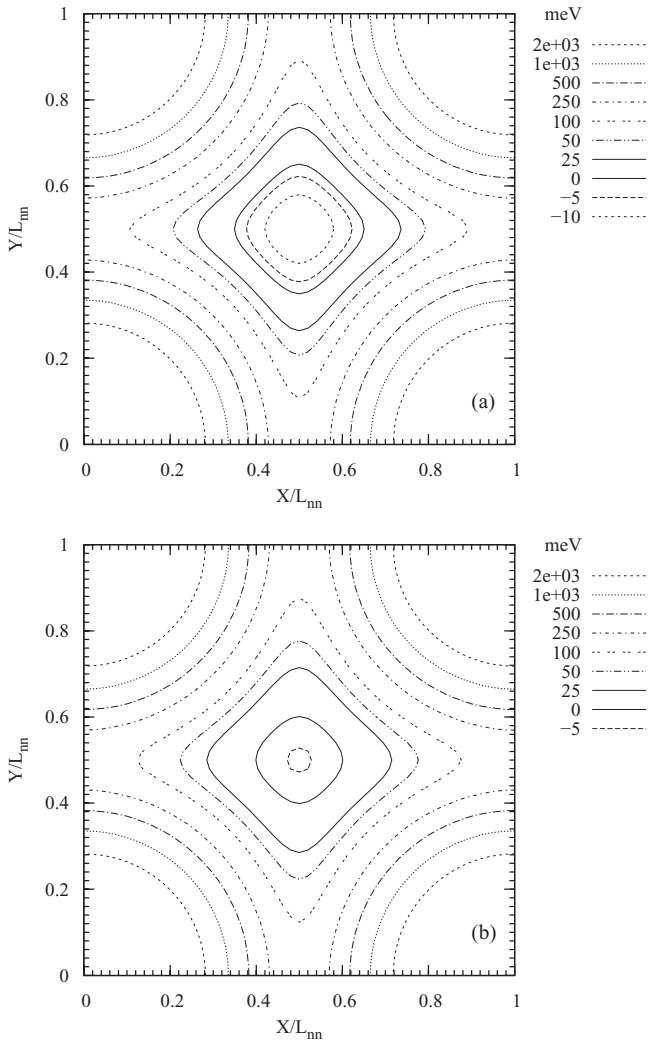

FIG. 1. 2D contour plots of the He-$p(1 \times 1)H_2$/KCl(001) potential energy surface for a unit cell at $z = 0$, the plane of the hydrogen molecules. The H_2 are at the corners of this square cell with side $L_{nn} = 4.44$ Å. (a) The contours for $DZL = 1.2$ Å with a potential energy of -13.3 meV at the center. (b) The contours for $DZL = 4.0$ Å with a potential energy of -5.4 meV at the center.

2. Wave packet

Equations (5) and (6) are solved with a wavepacket propagation scheme described in Ref. 5. Penetration of the wavepacket to the interlayer region now is included in all the calculations. The lateral motion is represented by plane waves, Eqs. (8) and (9), and the initial z-dependence of Ψ_0 is a Gaussian wavepacket. The values of the grid-size in the z-direction $\Delta z = 0.06$ Å and integration time-step $\Delta t = 0.04$ fs are as before. An absorbing potential at the large-z end of the z-grid enables long-time calculations (now 120 ps or more when there is transient trapping) that ensure that the scattering events go to completion and, with a determination of the He flux into the absorbing potential, an accurate account of the intensity in all diffraction and inelastic scattering channels is maintained.

The calculations are done with two initial wavepacket widths to give a sense of the effect of the averaging over excitation cross sections in the experiment. The width σ_z of the initial wavepacket is expressed in terms of the number NWI of gridpoints as $\sigma_z = \Delta z\, NWI/\sqrt{2}$. The choices $NWI = 600$ and $NWI = 100$ correspond to a somewhat finer or coarser energy resolution than in the He/H_2/NaCl(001) experiments. The increment in total energy that arises from the spread of the wavepacket is $\delta E = (\hbar/NWI\,\Delta z)^2/4m_a$ and is 2×10^{-4} meV for $NWI = 600$.

3. Scattering conditions

The excitation spectra of shear horizontal (SH) and longitudinal acoustic (LA) phonons are taken to be the $\omega(\mathbf{Q})$ fit in Paper III to the experiments[7] for $p(1 \times 1)$ H_2/NaCl(001).

Quite different scattering geometries are treated for the NaCl and KCl cases.

The scattering for $p(1 \times 1)$ H_2/NaCl(001) is evaluated for scan curve conditions[1] and a beam energy $E_i = 26.5$ meV as in the experiments. The scan curve has the outgoing beam in the plane of incidence with a fixed angle θ_{SD} ($= 90.1^\circ$ here) between the incident and outgoing beam. In the calculations the plane of incidence is at an angle $\phi \neq 0^\circ$ relative to the ΓM ($\hat{y}$) axis of the monolayer and the phonon **Q** is in that plane. For the $\phi = 0^\circ$ case and **Q** in the first Brillouin zone, there is no excitation of the SH mode.[4] SH–LA pairs of scattering events at three angles of incidence θ_i and $\phi = 1^\circ$ are treated in the present work. The diffraction conditions for a pair are the same, but the phonon excitations differ in order to satisfy the scan curve condition.

The scattering for $p(1 \times 1)$ H_2/KCl(001) is evaluated for $\phi = 1^\circ$ and several θ_i for specific SH and LA phonons without the scan curve constraint.

4. Approximating the Q-sum

The full one-phonon approximation in Eqs. (5)–(7) allows for the excitation of phonons at all wavevectors **Q** in the first Brillouin zone and thus, effectively, includes a continuum of wavevectors.[14] In the present work, we replace this continuum by single values of **Q** and polarization λ so that there are only two coupled equations, Eqs. (5) and (6), to be solved. The strength of the coupling $\tilde{V}_{\mathbf{Q},\lambda}$ depends on the number N of atoms in the monolayer as $1/\sqrt{N}$, Eq. (11) of Ref. 4. This implies that the norm of the wave function Ψ_1 for having excited a single specific phonon mode is $O(1/N)$ and very small. In an experiment, however, there are finite resolutions $d\mathbf{Q}$ in **Q** and $d\Omega$ in the solid angle Ω for the final direction of the scattered atom, so the experimental intensity includes a factor $N|\mathbf{Q}|d|\mathbf{Q}|d\Omega$ and the $1/\sqrt{N}$ dependence in $\tilde{V}_{\mathbf{Q},\lambda}$ is compensated. Our approximation of a single **Q** and λ and a specific value for N is a rough way of allowing for the experimental resolution in wavevector and solid angle. Larger values of N correspond to higher resolution and therefore to lower inelastic intensities.

We propagated the wavepacket with $N = 10$, to get total inelastic norms I_i of 0.1 to 0.2, and made a few calculations with $N = 5$ and $N = 20$ to test how results varied with this choice. For the data presented in Table I, I_i varies approximately as $1/N$, although the feedback to Ψ_0 leads to departures from an exact proportionality to $1/N$ at smaller N. Also, the conservation of total norm, Eq. (7), is maintained to within 0.1%.

5. Analysis

We characterize the results of the calculations using the elastic and inelastic norms $I_e \equiv (\Psi_0, \Psi_0)$ and $I_i \equiv (\Psi_1, \Psi_1)$ and channel norms, e.g., $I_i(\mathbf{g}) \equiv (S_{\mathbf{Q},\lambda}(\mathbf{g}), S_{\mathbf{Q},\lambda}(\mathbf{g}))$,

$$(S_{\mathbf{Q},\lambda}(\mathbf{g}), S_{\mathbf{Q},\lambda}(\mathbf{g})) \equiv \int_{-DZL}^{\infty} |S_{\mathbf{Q},\lambda}(\mathbf{g}, z, t)|^2 \, dz. \qquad (11)$$

TABLE I. Effect of the value of N on the self-consistent solution with coupling to only one phonon mode. Data for the $p(1 \times 1)$ H_2/KCl(001) model with $E_i = 15.1$ meV, $\theta_i = 20^\circ$, $DZL = 1.2$ Å, $NWI = 600$, and a longitudinal acoustic phonon mode with $Q = 0.718$ Å^{-1} and $\hbar\omega = 8.47$ meV. I_e and I_i are the total elastic and one-phonon inelastic norms; their sum should be 1 according to Eq. (7). The final column NI_i would be independent of N if I_i scaled as $1/N$ and this is nearly satisfied for $N = 10$ and 20.

N	I_e	I_i	$I_e + I_i$	NI_i
5	0.84741	0.15234	0.99975	0.7617
10	0.89527	0.10447	0.99974	1.0447
20	0.94047	0.05928	0.99975	1.1856

The partial norms $I_{e,i}$(trap) of Ψ_0 and Ψ_1 in the range $-DZL \leq z \leq 0$, defined by

$$I_e(\text{trap}) \equiv \int_{-\text{DZL}}^{0} \sum_{\mathbf{g}} |\psi_{\mathbf{g}}(z, t)|^2 \, dz \qquad (12)$$

with a similar definition for I_i(trap), are used to track the size and time evolution of the trapping in the interlayer region, as in Fig. 2 which is discussed in Sec. III B. Factors that are

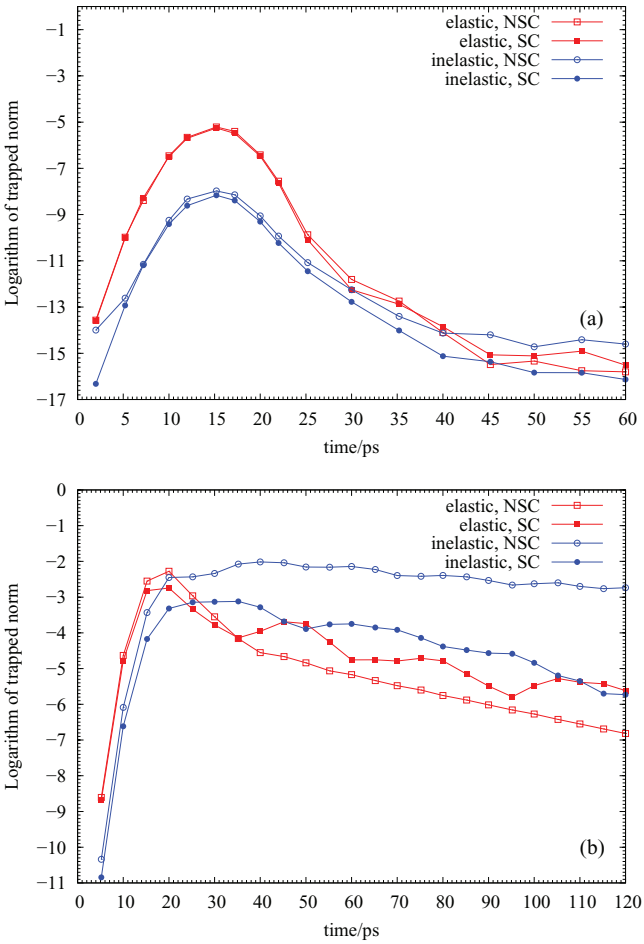

FIG. 2. The natural logarithms of the elastic and inelastic norms trapped between the planes of the KCl surface and the H_2 monolayer, as a function of time for the SC and NSC calculations. The norms of Ψ_0 and Ψ_1 for $-DZL < z < 0$ are evaluated for $\theta_i = 20^\circ$, $\phi = 1^\circ$, $E_i = 15.1$ meV, $NWI = 600$ (nearly a monochromatic beam), and SH phonons with $(Q, \omega) = (0.718$ Å^{-1}, 6.61 meV). (a) $DZL = 1.2$ Å. (b) $DZL = 4.0$ Å.

TABLE II. Total elastic and inelastic norms I_e and I_i at angle of incidence θ_i for scattering of 26.5 meV He atoms by the $p(1 \times 1)$ H_2/NaCl(001) monolayer as calculated[6] in Paper III (*NSC*) and here with the self-consistent solution. R_i is the ratio of the I_i for LA and SH phonons, I_i(LA)/I_i(SH). The stated phonons[a] are those for which the inelastic scattering satisfies the scan curve condition with $\theta_{SD} = 90.1°$. The azimuthal angle is $\phi = 1°$ relative to the ΓM axis of the monolayer, $N = 10$, and $NWI = 600$.

θ_i	46°	44.5°	37.2°
I_e(LA) (SC)	0.7407	0.7957	0.7111
I_e(SH) (SC)	0.9056	0.8872	0.9022
I_i(SH) (SC)	0.0941	0.1125	0.0975
R_i (SC)	2.753	1.814	2.959
I_i(SH) (NSC)[b,c]	0.114	0.141	0.117
R_i (NSC)	3.162	2.235	3.864
R_i(SC)/R_i(NSC)	0.871	0.810	0.766

[a](Q, ω) in Å^{-1} and meV for the SH phonons at $\theta_i = 46°$, 44.5°, and 37.2° are (0.865, 6.87), (0.6, 6.7), and (−0.6, 6.7) and for the LA phonons are (1.02, 8.27), (0.828, 8.69), and (−0.45, 7.83).
[b]By definition I_e(NSC) = 1; in practice I_e(NSC) departed from 1.00 by 0.5% at 46° and 1.2% at 37.2°. $I_e + I_i$ for the 6 SC calculations is maintained at 1.00 to within 0.04%.
[c]Values from the work of Paper III, obtained with $N = 1$, are restated here with $N = 10$.

applied to the channel norms to generate final elastic and inelastic intensities[6] in Paper III, i.e., a flux factor, the thermal average Debye-Waller factor, and an enhancement of phonon creation by scattering from thermally excited phonons, are not included in the present results. The SC approximation makes the *ad hoc* addition of that Debye-Waller factor at least partially redundant for this work. As before,[5] **g**-channels in Ψ_0 [Ψ_1] are said to be open when the parallel kinetic energy in that channel is less than the final atom energy in Ψ_0 [Ψ_1].

Because of the ambiguity in the choice of N for the single-**Q** approximation to the $\tilde{V}_{\mathbf{Q},\lambda}$ coupling, we present many of the results as ratios of norms where the prefactor N cancels. We use the ratio of the norms of the inelastic scattering for the LA and SH branches, $R_i \equiv I_i$(LA)/I_i(SH), and the ratio of the inelastic norm in the specular ($g = 0$) channel and the total inelastic norm in open channels, $I_{i,o}$, $F_i \equiv I_i(g = 0)/I_{i,o}$. These enable us to follow trends in the SC and NSC calculations in parallel and F_i is especially useful when the NSC calculation has a long-time loss in I_i arising from norm trapped in closed channels. This arises in $DZL = 4.0$ Å NSC cases for $p(1 \times 1)H_2$/KCl(001) in Sec. III B, where $I_{i,o}/I_i < 0.7$ for times long enough that most of I_i(SC) is in open channels, and we then use $I_{i,o}$(NSC) for comparisons to the SC results.

III. RESULTS

A. $p(1 \times 1)H_2$/NaCl(001)

SC versions of the NSC calculations of Paper III were performed for pairs of inelastic scattering at energy $E_i = 26.5$ meV, three angles of incidence $\theta_i = 46°, 44.5°,$ and 37° and azimuthal angle $\phi = 1°$. Table II shows the results of both versions of the calculations. The (Q, ω) of the SH and LA phonons that satisfy the scan curve condition at these θ_i are given in a footnote to Table II. The LA norm is much larger than the SH norm in each case, $R_i > 1$, and the trends with θ_i for the NSC calculation follow the SC results. However, the feedback term in the SC calculation leads to smaller ratios R_i and R_i(SC)/R_i(NSC) is in the range 0.77–0.87. The stronger LA scattering has a greater reduction in the final elastic SC norm, as shown by the values for I_e(LA) and I_e(SH) in the first two lines of Table II. This comparison of SC and NSC results involves two changes in the calculation: (1) the inclusion of penetration of Ψ_0 and Ψ_1 to the $-DZL < z < 0$ region and (2) the implementation of the self-consistency by including the $\tilde{V}_{\mathbf{Q},\lambda}$ term in Eq. (6) in the calculations. In a case where we treated the changes separately, the effect of the penetration was to change I_i by only about 1% and it gave a small part of the total change.

The SC calculations thus confirm the conclusions of Paper III for the trends and relative magnitudes of the inelastic scattering strengths. Including the small penetration to the interlayer region between the monolayer and substrate leads to an improved conservation of the wave function norm without major changes in the rest of the results.

B. $p(1 \times 1)H_2$/KCl(001)

The calculations for the $p(1 \times 1)H_2$/KCl(001) model are meant to explore what the consequences of a strong penetration to the interlayer region would be. We anticipated finding transient trapping of the elastic wave function Ψ_0 in the

TABLE III. Effect of the wavepacket width NWI for the $p(1 \times 1)$ H_2/KCl(001) model with $E_i = 15.1$ meV, $N = 10$, $DZL = 4.0$ Å, and SH mode with $(Q, \hbar\omega) = (0.718$ Å^{-1}, 6.61 meV). The total elastic and inelastic norms I_e and I_i, their sum, and the fractions $F_i = I_i(g = 0)/I_{i,o}$ are given. SC denotes results of the self-consistent calculations, Eqs. (5) and (6); NSC denotes results without the coupling term in Eq. (5). The SC–NSC pairs show a redistribution of strength caused by the mixing. The effect of changing NWI is much less in the SC calculation than in the NSC one.

	$NWI = 600$			$NWI = 100$		
θ_i	0°	15°	20°	0°	15°	20°
I_e (SC)	0.93406	0.94499	0.930475	0.92625	0.94223	0.93287
I_i (SC)	6.504×10^{-2}	5.340×10^{-2}	6.854×10^{-2}	7.301×10^{-2}	5.676×10^{-2}	6.619×10^{-2}
$I_i + I_e$ (SC)	0.99910	0.99840	0.99902	0.99926	0.99899	0.99906
F_i (SC)	3.92×10^{-3}	1.34×10^{-2}	3.67×10^{-2}	3.34×10^{-3}	1.69×10^{-2}	2.95×10^{-2}
$I_{i,o}$ (NSC)[a]	6.505×10^{-2}	0.220	0.111	0.118	0.186	0.287
I_i (NSC)	7.728×10^{-2}	0.426	0.165	0.181	0.288	0.514
F_i (NSC)	4.81×10^{-3}	4.22×10^{-2}	4.15×10^{-2}	5.41×10^{-3}	8.19×10^{-2}	5.60×10^{-2}

[a]These values are total inelastic norm in open channels.

TABLE IV. Dependence of total inelastic scattering norm in open channels $I_{i,o}$ on interlayer spacing DZL for the $p(1 \times 1)$ H_2/KCl(001) model at $E_i = 15.1$ meV, $\theta_i = 20°$, $N = 10$, and $NWI = 600$. SC, NSC, and F_i notation as in Table III; $R_{i,o} = I_{i,o}(\mathrm{LA})/I_{i,o}(\mathrm{SH})$. The phonon modes are the longitudinal acoustic and shear horizontal excitations at $Q = 0.718$ Å^{-1} with energies 8.47 and 6.61 meV, respectively.

	SC				NSC			
DZL (Å)	$I_{i,o}$(SH)	$R_{i,o}$	F_i(SH)	F_i(LA)	$I_{i,o}$(SH)	$R_{i,o}$	F_i(SH)	F_i(LA)
1.2	0.0686	1.53	0.0133	0.0055	0.0978	1.49	0.0135	0.0188
2.8	0.0800	2.25	0.0477	0.103	0.0894	2.40	0.0046	0.0967
4.0	0.0679	1.81	0.0359	0.0755	0.111	5.88	0.0415	0.127

interlayer region and that the time scale for the escape would be long. The first calculations were with the (NSC) wavepacket propagation used in Paper III and showed trapping of Ψ_0 that persisted 50–100 ps for the $DZL = 2.8$ and 4.0 Å cases. However, the inelastic wave function Ψ_1 had a large component in the interlayer region that mostly did not escape to large z, as shown by the evolution of the open-channel norm $I_{i,o}$. At $\theta_i = 15°$ and 20°, much of the inelastic norm simply "disappeared" as time increased and the last term in Eq. (6) then acted more as a "sink" than a "source." This observation led us to the present self-consistent theory that includes the coupling term in the Ψ_0 propagation. The transient trapping involves a strong mixing of the Ψ_0 and Ψ_1 components of the total wave function because the coupling terms are large in the interlayer region. This results in a reduction of the inelastic norm and the mixing modifies the distribution over channels in Ψ_0.

The scattering for $p(1 \times 1)$ H_2/KCl(001) was evaluated for two examples of one-phonon creation events, a SH phonon of $(Q, \omega) = (0.718$ Å^{-1}, 6.61 meV) and a LA phonon of $(Q, \omega) = (0.718$ Å^{-1}, 8.47 meV). These are phonons from the spectrum[7] of $p(1 \times 1)$ H_2/NaCl(001); the experimental data for the SH event at $E_i = 15.1$ meV were shown in Paper III. Most of the calculations were for initial energy $E_i = 15.1$ meV and trends were followed as a function of the angle of incidence θ_i, effective interlayer spacing DZL, and wavepacket width NWI.

Table III shows that the total inelastic norm in the SC solution, I_i(SC), changes by about 10% as NWI is increased at three angles θ_i. This is very different from the NSC results I_i (NSC), where the changes with NWI are much larger. [These comparisons are sensitive to whether the closed-channel contributions are included. The NSC ratios are $I_{i,o}(NWI = 600)/I_{i,o}(NWI = 100)\{I_i(NWI = 600)/I_i(NWI = 100)\} = 1.18\{1.48\}$ at $\theta_i = 15°$ and 0.33 $\{0.39\}$ at $\theta_i = 20°$.] The mixing in the interlayer region reduces the sensitivity to NWI in the SC calculations. At long times, 80–100 ps after the turning-point time of the wavepacket [when the expectation value $(\Psi_0, z\Psi_0)/(\Psi_0, \Psi_0)$ is minimum], more than 90% of I_i is in open channels for the SC solution but only 55%–65% is in open channels for the NSC one.

Examples from a series of calculations to explore the dependence on the interlayer width DZL are given in Table IV for $\theta_i = 20°$. The relative strength of the LA excitation to the SH excitation, R_i, is larger for larger values of DZL in the NSC calculations. This monotonic behavior is not found in the SC calculations, for which R_i is largest at $DZL = 2.8$ Å. We use F_i, the fraction of $I_{i,o}$ that is in the specular channel, to examine how the distribution over channels changes in the SC solution. A comparison of the SC and NSC columns for $DZL = 2.8$ Å shows large changes in the ratios; the trends with DZL are quite uneven though. The feedback reduces the total inelastic norm; I_i(SH) is smaller for SC than for NSC. There also is a large effect on the trapped norms, as shown in Fig. 2.

We made a few calculations at other incident energies to show the generality of the trapping and of the self-consistent mixing of Ψ_0 and Ψ_1 in the interlayer region. Some results are given in Table V. For a low incident energy $E_i = 10$ meV, comparable to the energy 8.47 meV of the

TABLE V. Inelastic scattering results at energies $E_i = 10$ meV (LA excitation) and $E_i = 26.5$ meV (SH excitation), phonon modes as in Table IV. H_2/KCl(001) model for $\theta_i = 20°$, $N = 10$, and $NWI = 600$. Comparisons of SC and NSC calculations at two times t long after the turning-point time (19.5 ps at 10 meV and 11.8 ps at 26.5 meV).

	$E_i = 10$ meV, LA				$E_i = 26.5$ meV, SH			
	SC		NSC		SC		NSC	
t(ps)	120	180	120	180	50	98	50	98
I_i	6.20×10^{-2}	6.15×10^{-2}	7.58×10^{-2}	7.77×10^{-2}	0.148	0.141	0.950	1.043
I_i (closed)[a]	6.54×10^{-4}	1.06×10^{-4}	7.29×10^{-3}	8.84×10^{-3}	9.09×10^{-3}	1.26×10^{-3}	7.15×10^{-2}	7.54×10^{-2}
I_e (trap)[b]	7.24×10^{-4}	1.50×10^{-4}	1.97×10^{-3}	1.38×10^{-3}	5.84×10^{-3}	3.72×10^{-4}	4.05×10^{-3}	2.77×10^{-4}
I_i(trap)[b]	7.66×10^{-4}	1.10×10^{-4}	7.98×10^{-3}	9.17×10^{-3}	1.23×10^{-2}	8.11×10^{-4}	0.185	9.98×10^{-2}
$I_i(g = 0)$	1.40×10^{-2}	1.41×10^{-2}	1.85×10^{-2}	1.88×10^{-2}	2.45×10^{-3}	2.46×10^{-3}	1.45×10^{-2}	1.50×10^{-2}
F_i	0.229	0.229	0.270	0.272	1.77×10^{-2}	1.76×10^{-2}	1.65×10^{-2}	1.55×10^{-2}

[a] $I_i(\mathrm{closed}) = I_i - I_{i,o}$ is the partial norm of Ψ_1 in closed channels, those with parallel kinetic energy greater than the final energy of the atom $E_f = E_i - \hbar\omega(Q)$.
[b] Partial norms of Ψ_0 and Ψ_1 in the range $-DZL < z < 0$, i.e., in the interlayer region.

TABLE VI. Trends of the inelastic scattering for the $p(1 \times 1)$ H_2/KCl(001) model at $E_i = 15.1$ meV, with $N = 10$ and $NWI = 600$, except as noted. SC solutions for SH and LA excitations as in Table IV. The norm of total inelastic scattering in open channels $I_{i,o}$ and that in the specular channel $\mathbf{g} = 0$ are given.

		SH		LA	
DZL Å	θ_i	$I_{i,o}$	$I_i(g=0)$	$I_{i,o}$	$I_i(g=0)$
1.2	0°	0.1328	4.14×10^{-5}	0.1317	1.02×10^{-3}
	20°[a]	6.86×10^{-2}	9.10×10^{-4}	0.1045	5.72×10^{-4}
2.8	0°[b]	8.64×10^{-2}	3.50×10^{-4}	9.50×10^{-2}	1.48×10^{-2}
	20°	8.00×10^{-2}	3.82×10^{-3}	0.180	1.86×10^{-2}
4.0	0°	6.41×10^{-2}	2.51×10^{-4}	8.94×10^{-2}	1.28×10^{-2}
	15°	5.07×10^{-2}	6.79×10^{-4}	9.97×10^{-2}	5.45×10^{-3}
	20°	6.79×10^{-2}	2.49×10^{-3}	0.1220	9.22×10^{-3}

[a]For the H_2/NaCl(001) model at these scattering conditions the SH values are 4.72×10^{-2} and 4.75×10^{-4}, respectively.
[b]$NWI = 100$ for this case.

created LA phonon, a large fraction ≈0.25 of $I_{i,o}$ is in the specular channel. The persistence of I_i(trap) is much greater for the NSC calculation than for the SC one, as shown both by the amount in closed channels I_i(closed) and by that specifically trapped in the interlayer region I_i(trap), Fig. 3. The time dependence for I_i(trap) of the LA phonon in Fig. 3 is similar to that of the SH phonon in Fig. 2(b). The persistence of I_i(trap) is also much greater in the NSC calculation at $E_i = 26.5$ meV. At that energy, I_i(NSC) is close to 1, which shows a clear failure to maintain a reasonable account of the total norm.

In addition to determining the trapped norms of Ψ_0 and Ψ_1, we have analyzed the trapped probability density as a function of time and distance from the H_2 monolayer. We evaluate $|\Psi_0|^2$ in several z-planes for $-DZL < z < 0$ and then calculate the average positions $\langle x \rangle$ and $\langle y \rangle$ and their variances σ_x and σ_y as a function of time in these planes. Figure 4 has examples of contour plots of the $|\Psi_0|^2$ in the planes $z = -1.0$ Å and $z = -2.44$ Å, evaluated 20 ps after the turning-point time of the wavepacket in an SC calculation with $E_i = 15.1$ meV, $\theta_i = 15°$, $NWI = 600$, $DZL = 4.0$ Å, and creation of SH phonons with $(Q, \omega) = (0.718$ Å^{-1}, 6.61 meV). The contour plots largely reflect the symmetry of the square cell. The lateral extent of $|\Psi_0|^2$ near the H_2 layer, Fig. 4(a) ($z = -1.0$), is smaller than further away, Fig. 4(b) ($z = -2.44$), due to the short-range repulsive interaction of He with H_2 at the unit cell corners. Figure 5 shows the average positions $\langle x \rangle$, $\langle y \rangle$ and their variances σ_x and σ_y in the plane $z = -1.90$ Å as a function of time. The large variances demonstrate that the probability density is spread widely over the plane; if the distributions were uniform, the variance would be $L_{nn}/\sqrt{12}$ (=1.28 Å for

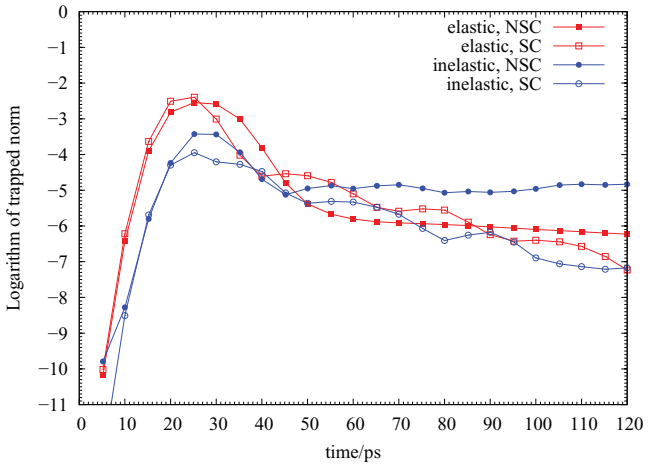

FIG. 3. The natural logarithms of the trapped elastic and inelastic norms, defined as in Fig. 2, as a function of time for the SC and NSC calculations. The scattering event has $\theta_i = 20°$, $\phi = 1°$, $E_i = 10.0$ meV, $NWI = 600$, $DZL = 4.0$ Å, and LA phonons with $(Q, \omega) = (0.718$ Å^{-1}, 8.47 meV).

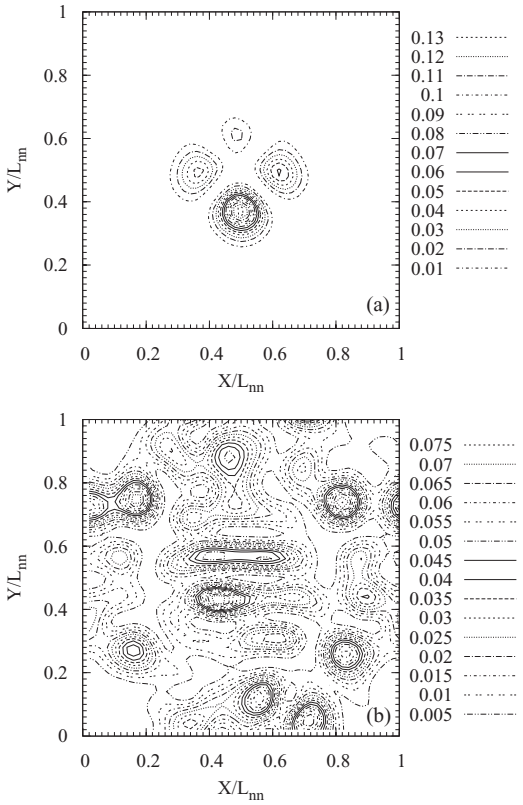

FIG. 4. 2D contour plots of $|\Psi_0|^2$ in the interlayer region from an SC calculation for a scattering event with $E_i = 15.1$ meV, $\theta_i = 15°$, $NWI = 600$, $DZL = 4.0$ Å, and SH phonons with $(Q, \omega) = (0.718$ Å^{-1}, 6.61 meV). Evaluated in two planes at 20 ps after the turning point time of the wavepacket, with trapped elastic norm about 50% of its maximum value. (a) $z = -1.0$ Å. (b) $z = -2.44$ Å.

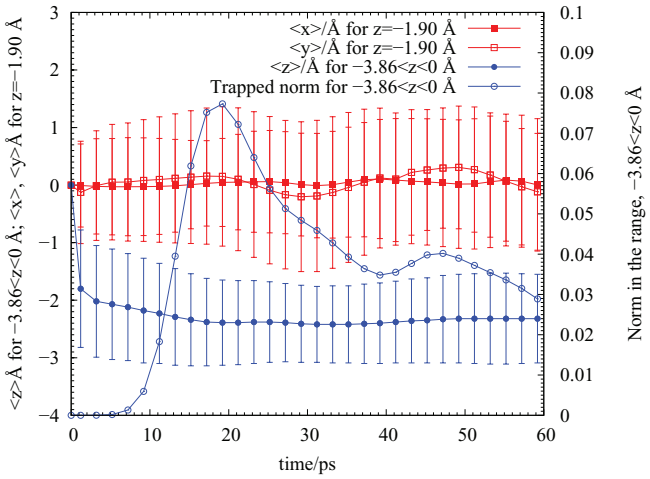

FIG. 5. The average positions in the x and y directions, $\langle x\rangle$, $\langle y\rangle$, and their variances (error bars) as function of time in the plane $z = -1.90$ Å, evaluated with $|\Psi_0|^2$ of the same scattering event as in Fig. 4. Also shown are the average position in the z direction, $\langle z\rangle$, calculated for $|\Psi_0|^2$ on the interval $-DZL < z < 0$ and the trapped elastic norm (right ordinate axis) to set the time relative to the evolution of the scattering event. The turning-point time is at 15.32 ps and the trapped elastic (inelastic) norm is maximum at 18.8 (19.6) ps.

the KCl case) and this is the scale shown in the figure. Also shown are the average $\langle z\rangle$ and trapped elastic norm for $-DZL < z < 0$ to show the relation of the time-dependence of the other averages to the evolution of the scattering event. The averages and their variances have little time dependence, although the total trapped norm decreases from 0.08 at its maximum to 0.03 at the largest time in the figure. A rather uniform distribution is established early in the scattering event and is maintained even when I_e(trap) has decayed to 1/3 of its maximum value. After a transient period, $\langle z\rangle$ is practically time-independent. We interpret these data as showing that multiple scattering of the He atom between the substrate and the hydrogen layer effectively establishes a stationary distribution with a normalization that follows I_e(trap). However, the variances σ_x and σ_y depend on DZL and are smaller for $DZL = 1.2$ and 2.8 Å (not shown) than for the 4.0 Å case shown here, which is consistent with the distributions in Fig. 4.

Our original goal was to examine the effects of penetration of the He atom to the interlayer region. In Table VI we give our best estimate for trends of the inelastic scattering with DZL and θ_i. The relative strength of total LA inelastic scattering to that of the SH, R_i, increases with increasing thickness of the interlayer region mostly because of an increase in the absolute strength for the LA.

IV. CONCLUSIONS

We conclude that the effects of interlayer trapping are seriously overestimated without the self-consistent solution. This is another manifestation of the strong-coupling scattering of thermal energy He atoms. The portion of the wave function that penetrates to the interlayer region experiences strong elastic and inelastic scattering. However, the trapping keeps the inelastic wave there long enough that the coupling to the phonons restores much of the lost energy and transforms much of this part of the inelastic wave back to the elastic component. The final inelastic strength remains large, but is not as large as estimated without allowing for the feedback, and the distribution over elastic channels is much changed by the penetration and trapping.

The self-consistent solutions reported here are based on a serious simplification of the formalism, to only one phonon excitation (one $\mathbf{Q}$ and polarization). To do calculations with a sampling of 25 or so points in the Brillouin zone will require considerably more computational resources than we now have, but this extension does seem feasible in the light of the expanding capabilities of parallel computation for such a problem and work is in progress.

The problem of combining diffractive and inelastic scattering in an internally consistent theory is of long standing and is particularly difficult when both types of scattering are strong. This is the situation here, with a target that is highly corrugated to the extent that the He atoms may penetrate it. The energy ranges we treat are intermediate between very low energies, where one-phonon losses would suffice to trap the incoming atom,[20] and higher energies, where multiphonon processes dominate the inelastic scattering. Perhaps surprisingly, we find that the self-consistent formulation of the one-phonon inelastic scattering moderates the sensitivity of the calculations to details such as the width of the wave packet. The next stages in the development of the theory should give new insights into the scattering effects that are summarized in empirical Debye-Waller factors.

APPENDIX: GEOMETRICAL OPTICS APPROXIMATION

As a guide to interpreting the penetration of the elastic wave function Ψ_0 to the space between the monolayer and the substrate, we construct a geometrical optics approximation for the propagation of rays incident on the potential energy surface from above (positive z). Determining which rays are able to pass through the "hole" in the $z = 0$ plane, allowing for multiple reflections, gives the transmitting fraction of the unit cell as a function of incident angle θ_i. This fraction decreases monotonically as θ_i increases. The trapped norm I_e(trap) in the wavepacket calculation has more complex dependence on θ_i. However its maximum has a large decrease from 0° to 43° and 75°, in qualitative agreement with the ray tracing results. This is remarkable because the calculation of the transmitted rays does not include such effects as the multiple scattering of rays in the interlayer region, details of the potential energy surface there, and the role of attractive forces on the atom at $z > 0$.

The ray tracing is done in a mid-plane at $y = L_{nn}/2$ of the square unit cell illustrated in Fig. 1. The $x - z$ surface of potential energy equal to the incident atom energy E_i is constructed, using $E_i = 15.1$ meV and $DZL = 1.2$ and 4.0 Å for H_2/KCl(001) and 26.5 meV and $DZL = 1.2$ Å for H_2/NaCl(001). Then rays incident at angle θ_i relative to $\hat{z}$ at a specified position x are traced through successive geometric reflections (angle of incidence at the surface equal to angle of reflection) to determine whether they are transmitted "down" through the $z = 0$ plane or are reflected "up" away from the surface. Up to 8 successive reflections at the surface

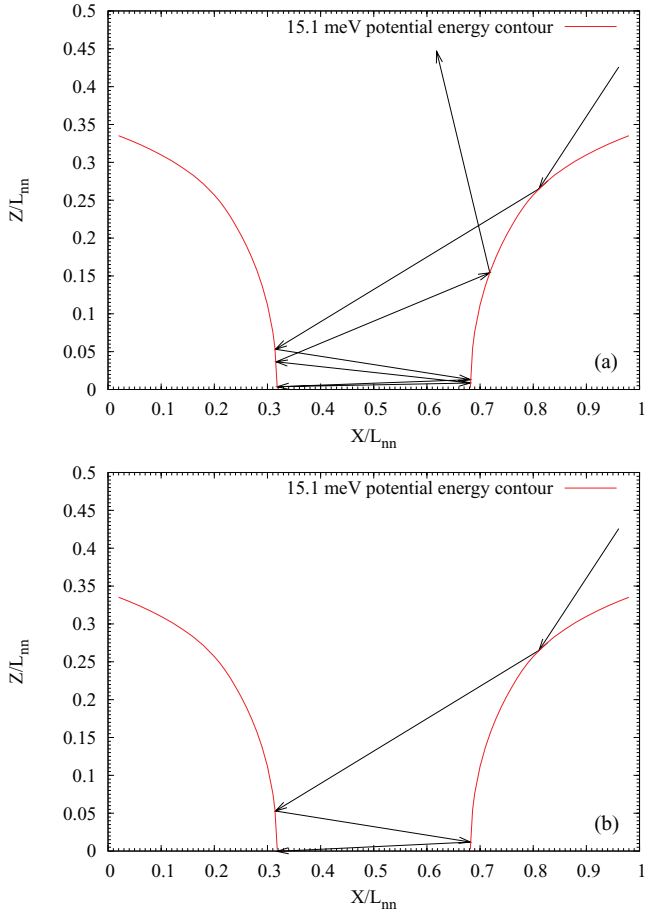

FIG. 6. Examples of ray tracing in which the incident ray is reflected without reaching $z = 0$ and in which it reaches the $z = 0$ plane after multiple reflections ("transmitted"). Angle of incidence $\theta_i = 43^\circ$ and first contact of ray with reflecting surface is x_0/L_{nn}. The arrows denote the direction of the ray. H_2/KCl(001) model with $L_{nn} = 4.44$ Å, $DZL = 4.0$ Å, and $E_i = 15.1$ meV. (a) Reflection, $x_0/L_{nn} = 0.8110$. (b) Transmission, $x_0/L_{nn} = 0.81094$. The edge x_e of the transmitting strip is at $x_e/L_{nn} \simeq 0.811$.

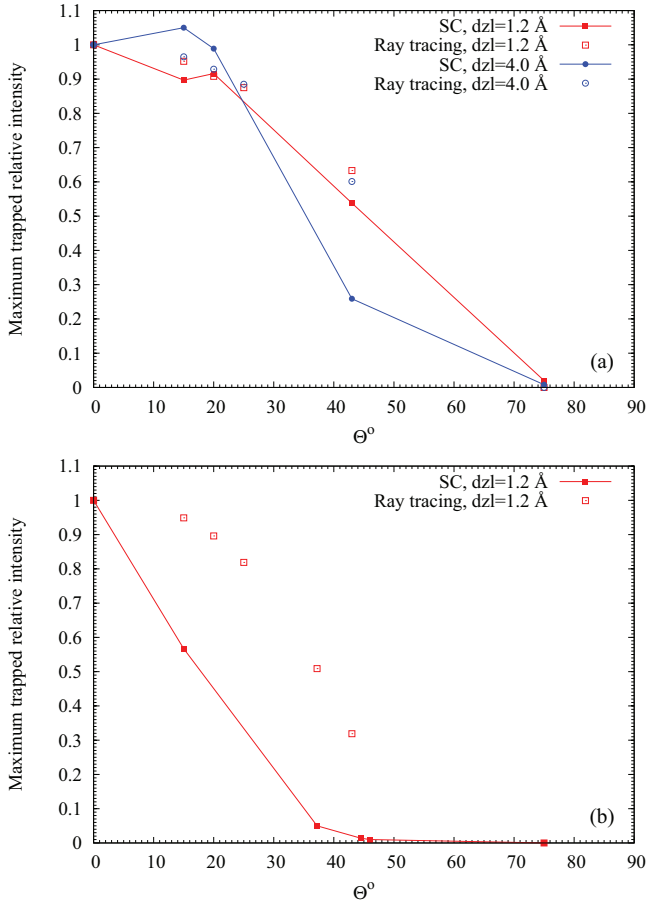

FIG. 7. The ratio w_w of the maximum trapped elastic norm for wavepacket incident at θ to that at $\theta = 0^\circ$ and the ratio w_r of the ray-tracing transmitted fraction at θ to that at $\theta = 0^\circ$. SC calculations for the specified event. (a) KCl, $E_i = 15.1$ meV, $NWI = 600$, $\phi = 1^\circ$, and SH phonon (0.718 Å^{-1}, 6.61 meV). (b) NaCl, $E_i = 26.5$ meV, $NWI = 600$ $\phi = 1^\circ$, and SH phonons as in Table II for 37.2°, 44.5°, and 46°. For the other angles, SH phonon with (0.685 Å^{-1}, 6.87 meV). For $\theta = 75^\circ$ all ray tracing results gave zero which is difficult to see in the graph because the points are on top of each other.

are evaluated for a given incident ray and this is enough to assign the ray as transmitted or reflected and determine the edges x_e of the transmitting strip to $\pm 0.001 L_{nn}$. Two examples are shown in Fig. 6. For the angle of incidence shown there, $\theta = 43^\circ$, the edge of the transmitting strip is at $x_e/L_{nn} \simeq 0.811$. Rays with impact position farther from the "hole" are reflected while those closer to the "hole" are transmitted. We present the result for the transmitting width $\Delta x_e(\theta)$ in Fig. 7 in the form of the ratio $w_r = \Delta x_e(\theta)/\Delta x_e(0)$.

As a measure of the amount of wavepacket transmitted in the scattering calculations, we follow the trapped elastic norm as a function of time and use the maximum value. This depends on the potential energy surface at $z < 0$, the inelastic scattering (SH or LA), and the width NWI as well as on θ, so we compare trends within one series set by DZL, NWI, and the phonon. Results for the ratio w_w between the maximum trapped elastic norm at θ_i and the maximum trapped norm at $\theta = 0^\circ$ are plotted in Fig. 7. There are two KCl series and one NaCl series of angles θ_i. There is qualitative agreement between the trends for w_r and w_w in the three series. The ray tracing ratios decrease monotonically to very small values as θ_i increases while the wavepacket ratios have an intermediate maximum at $15^\circ - 20^\circ$ for the KCl series and then decrease more sharply than in the ray-tracing. We note that the ray tracing results in most cases are larger than the wavepacket results probably because the ray tracing does not include effects such as impedance mismatching that arise in wave propagation. There are large quantitative differences with the ratios obtained from the NSC calculations ($NWI = 100$, KCl(001) cases) where maxima of 1.3–1.7 are found; i.e., the NSC approximation is misleading also for this aspect of the trapping.

[1]A. P. Graham, Surf. Sci. Rep. **49**, 115 (2003).
[2]L. W. Bruch, R. D. Diehl, and J. A. Venables, Rev. Mod. Phys. **79**, 1381 (2007), and references contained therein.
[3]B. Gumhalter, Phys. Rep. **351**, 1 (2001); J. Phys.: Condens. Matter **24**, 104015 (2012).
[4]L. W. Bruch and F. Y. Hansen, J. Chem. Phys. **122**, 114714 (2005). (Denoted as Paper I.)
[5]F. Y. Hansen and L. W. Bruch, J. Chem. Phys. **127**, 204708 (2007). (Denoted as Paper II.)
[6]L. W. Bruch, F. Y. Hansen, and F. Traeger, J. Chem. Phys. **134**, 194308 (2011). (Denoted as Paper III in the text.) The channel norms denoted by N with subscripts in Papers I–III are denoted by $I_{...}$ here.
[7]F. Traeger, Ph.D. dissertation, Max-Planck-Institut für Strömungsforschung and Universität Göttingen, Göttingen, Germany, 2001; F. Traeger and J. P. Toennies, J. Phys. Chem. B **108**, 14710–14725 (2004); J. P. Toennies and F. Traeger, J. Phys.: Condens. Matter **19**, 305009 (2007).

[8]F.-M. Tao, J. Chem. Phys. **100**, 4947–4954 (1994).
[9]D. Spelsberg and W. Meyer, J. Phys. Chem. **100**, 14637–14642 (1996).
[10]M. C. Vargas and W. L. Mochán, Surf. Sci. **406**, L619–L620 (1998); **409**, 130–136 (1998).
[11]R. D. Diehl, T. Seyller, M. Caragiu, G. S. Leatherman, N. Ferralis, K. Pussi, P. Kaukasoina, and M. Lindroos, J. Phys.: Condens. Matter **16**, S2839–S2862 (2004).
[12]B. H. Choi and R. T. Poe, J. Chem. Phys. **83**, 1330 (1985).
[13]R. Manson and V. Celli, Surf. Sci. **24**, 495 (1971).
[14]A. Šiber and B. Gumhalter, Phys. Rev. B **71**, 081401 (2005).
[15]D. Eichenauer and J. P. Toennies, J. Chem. Phys. **85**, 532 (1986).
[16]A. Šiber and B. Gumhalter, J. Phys.: Condens. Matter **20**, 224002 (2008).
[17]S. Daon, E. Pollak, and S. Miret-Artés, J. Chem. Phys. **137**, 201103 (2012).
[18]J. Heidberg, A. Voßberg, M. Hustedt, M. Thomas, S. Briquez, S. Picaud, and C. Girardet, J. Chem. Phys. **110**, 2566–2578 (1999).
[19]L. W. Bruch, M. W. Cole, and E. Zaremba, *Physical Adsorption: Forces and Phenomena* (Dover, Mineola, NY, 2007).
[20]A. Šiber, B. Gumhalter, and C. Wöll, J. Phys.: Condens. Matter **14**, 5913 (2002).